Available online at www.sciencedirect.com
SCIENCE DIRECT®
Journal of Sound and Vibration 284 (2005) 151–172
JOURNAL OF SOUND AND VIBRATION
www.elsevier.com/locate/jsvi

Non-linear dynamic analysis of a multi-mesh gear train using multi-term harmonic balance method: period-one motions

A. Al-shyyab[a], A. Kahraman[b,*]

[a]*The University of Toledo, Toledo, OH 43606, USA*
[b]*Department of Mechanical Engineering, The Ohio State University, 206 W. 18th Avenue, Columbus, OH 43210, USA*

Received 23 May 2003; accepted 9 June 2004

Abstract

A non-linear time-varying dynamic model of a typical multi-mesh gear train is proposed in this study. The physical system includes three rigid shafts coupled by two gear pairs. The lumped parameter dynamic model includes the gear backlash in the form of clearance-type displacement functions and parametric variation of gear mesh stiffness values dictated by the gear contact ratios. The system is reduced to a two-degree-of-freedom definite model by using the relative gear mesh displacements as the coordinates. Dimensionless equations of motion are solved for the steady-state period-1 response by using a multi-term Harmonic Balance Method (HBM) in conjunction with discrete Fourier Transforms and a Parametric Continuation scheme. The accuracy of the HBM solutions is demonstrated by comparing them to direct numerical integration solutions. Floquet theory is applied to determine the stability of the steady-state harmonic balance solutions. An example gear train is used to investigate the influence of key system parameters including alternating mesh stiffness amplitudes, gear mesh damping, static torque transmitted, and the gear mesh frequency ratio.

1. Introduction

Under loaded dynamic conditions, gear systems often exhibit dynamic gear mesh forces that can be much larger than static forces transmitted. These dynamic forces that consist of high-

*Corresponding author. Tel.: +1-614-292-4678, fax: +1-614-292-3163.
E-mail address: kahraman.1@osu.edu (A. Kahraman).

0022-460X/$ - see front matter © 2004 Elsevier Ltd. All rights reserved.
doi:10.1016/j.jsv.2004.06.010

Nomenclature

b	half of clearance (backlash)
c	damping coefficient
e	gear motion transmission error
f	external force
g	discontinuous displacement function
HBM	Harmonic Balance Method
I	polar mass moment of inertia
$\mathbf{J}$	Jacobian matrix
k	gear mesh stiffness
$\mathbf{M}$	Monodromy matrix
m	mass
n	mesh frequency ratio ($n = Z_2/Z_3$)
NI	numerical integration
p	relative gear mesh displacement
Q	number of discrete time points
q	discrete time interval
R	number of harmonic components considered in the solution
r	radius
$\mathbf{S}$	matrix form of non-linear algebraic equation set
T	torque
t	time
u	displacement harmonic amplitude
$\mathbf{U}$	displacement vector
v	describing function
Z	number of gear teeth
δ	Kronecker delta
Λ	dimensionless frequency
κ	dimensionless mesh stiffness
$\hat{\lambda}$	control parameter
θ	rotational displacement
ω	characteristic frequency
Ω	nominal rigid-body angular velocity
ζ	damping ratio

Subscripts

a	alternating component
c	characteristic quantity
eq	equivalent
i	gear index
m	mean component
ni	ith natural mode

Superscripts

ℓ	gear mesh index ($\ell = 1, 2$)
rms	root-mean-square value
T	matrix transpose

frequency gear mesh harmonic orders must be balanced at the bearing supports and are eventually transmitted to the housing to act as the main excitations for gear related noise. In addition, cyclic dynamic loading experienced by the gear teeth impacts the fatigue life of the gear systems directly. Therefore, a better understanding of the gear system dynamics is viewed as crucial to designing products at acceptable noise levels and fatigue lives. One such common gear system, a multi-mesh gear train that is formed by three shafts and two gear pairs whose dynamic model is shown in Fig. 1, is considered in this study. The shaft in the middle holds two separate gears, each forming a mesh with another gear held by another shaft. This system finds its applications in automotive, aerospace, marine and industrial products. For instance, in automotive applications, this gear set arrangement is used commonly as the final drive unit of transverse, front-wheel-drive automatic transmissions, manual transmissions, and continuously-variable transmission final drive units. The main focus of this study is on the nonlinear dynamic behavior of such gear systems.

1.1. Literature review

A large number of gear dynamic studies were performed in the past for various purposes. As a review paper by Ozguven and Houser [1] and detailed literature survey of Blankenship

and Singh [2] indicate, gear dynamics models vary in many aspects ranging from the configuration analyzed, effects and degrees of freedom included, types of excitations considered and the solution methodologies employed. In Refs. [3,4], it was stated and shown experimentally that a spur gear pair exhibits a nonlinear, time-varying behavior due to the gear backlash nonlinearity (piecewise-linear) and the periodically time-varying gear mesh stiffness. The single pair models published to date can be classified in four groups based on their ability in incorporating these two key attributes, i.e. gear backlash nonlinearity and time-varying mesh stiffness: (1) linear, time-invariant (LTI) models that neglected both tooth separations caused by gear backlash and variations in gear mesh stiffness, (2) linear, time-varying (LTV) models that included only a time-varying mesh stiffness, (3) nonlinear time-invariant (NTI) models that considered gear backlash, but not time-varying parameters, and (4) nonlinear time-varying (NTV) models having both effects included. Published experimental data [4,5] states that the resultant dynamic behavior of a spur gear pair can only be described by a NTV model.

In view of the same classification, published dynamic models for the multi-mesh system considered in this study (Fig. 1) fall mostly under LTI [6–14] or LTV [15–18] models. As the LTI models employed a standard eigen value solution combined with the modal summation technique yields both free and forced vibration characteristics of the gear system, a large number of degrees of freedom were allowed in these models. Therefore, they were able to include several effects that existed in the actual system such as coupled-transverse-torsional-axial motions of the helical gear systems, and detailed shaft and bearing formulations. For instance, Iida et al. [9] neglected the meshing stiffness fluctuations and tooth separations, while allowing the counter shaft in the middle to have both flexural and torsional motions. The solutions for the natural frequencies and the mode shapes were found using modal analysis, the effect of the angle between power transmission lines was investigated. In a later work, Iida et al. [10] performed a similar torsional-lateral analysis of the same system. This time, the counter shaft was considered rigid with elastic support bearings, and the analytical solutions for this limiting case were compared to experiments. Lim and Li [8] developed a multi-mesh counter-shaft geared rotor model with six-degree-of-freedom (sdof) motion for each rigid gear wheel. The linearized equations of motion applied to double mesh geared rotors. The damping coefficients were defined in terms of the modal coefficients. The effects of the angles between the power transmission lines on the overall dynamic response were shown. A general shaft finite element formulation was applied to the same system to study coupled shaft, bearing and gear vibrations [14].

The linear, time-varying investigations of the physical system of Fig. 1 focused primarily on the stability of the parametrically excited system. As one of the earlier LTV gear system models, Benton and Seireg [16] used the phase plane method to solve for a time-varying gear mesh coupling. Sinusoidal and rectangular functions were considered as extreme cases of mesh stiffness variations. It was predicted that gear systems could exhibit primary and sub-harmonic resonances resulting in regions of unstable motions. The stability and solution was analyzed for extreme cases of mesh excitations mentioned earlier. Mollers [17] presented stability maps that define the ranges of unstable motions as a function of gear mesh damping and mesh stiffness amplitudes. Most recently, Lin and Parker [18] proposed solution based on the Method of Multiple Scales to obtain the response of the system. Their stability analysis suggested that parametric instabilities are

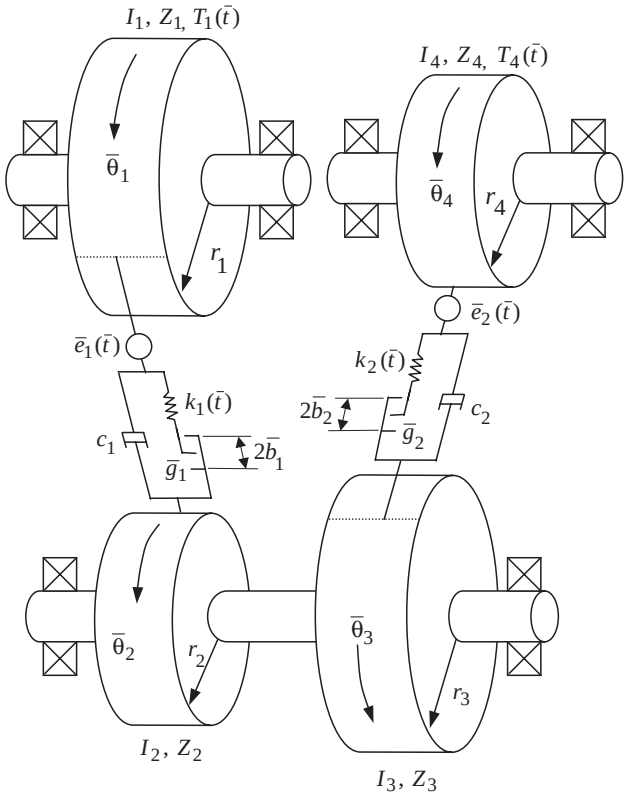

Fig. 1. Dynamic model of the physical system.

possible near the primary and fundamental resonance frequencies as well as at the combination frequencies.

1.2. Scope and objectives

As the LTV models can effectively point out the regions of large vibrations, their predictions regarding unstable motions are somewhat misleading. Experimental studies demonstrate that, as vibration amplitudes increase significantly, the tooth separations (loss of contact) occur resulting in a softening type behavior with bounded stable motions instead of unstable ones [4,5,13,19]. In addition, many other experimentally observed nonlinear phenomena exhibited by this type of systems [13,20] are yet to be fully described. Accordingly, the main objective of this study is to develop a multi-degree-of-freedom NTV model of the physical systems as shown in Fig. 1 to investigate the influence of nonlinear and time-varying parameters on the dynamic response. The analytical solutions for the steady-state response of the system will be obtained by using a multi-term HBM formulation. Harmonic balance solutions will be verified by comparing them to those of numerical simulation. Detailed parametric studies will be performed to investigate the sensitivity of the nonlinear dynamic behavior to each key system parameter including alternating

mesh stiffness amplitude, mesh damping, mean load transmitted, and the ratio of mesh frequencies.

Since the focus is on the nonlinear behavior, a minimum number of degrees of freedom will be utilized in the model in the form of torsional displacements. Accordingly, shaft and bearing flexibilities will be ignored. Also only period-1 motions will be considered in this study while the sub-harmonic motions are investigated in a companion paper [21]. The stability of the steady-state period-1 solutions will be determined by using the Floquet theory.

2. Dynamic model formulation

2.1. The physical system and the dynamic model

Behavior of the dynamic model of the physical system shown in Fig. 1 is the main focus of this study. The system consists of two separate gear meshes. Four gears mounted on three shafts form this gear train. It consists of two gear pairs mounted on rigid bearings and shafts. The following assumptions are employed in this model: (1) The shafts are assumed to be rigid such that no deflection in any direction is possible. (2) Gears are connected to the shafts rigidly. (3) Gear blanks (rims) are assumed to be rigid, only gear flexibility is possible at the gear mesh via representative mesh stiffness. (4) Bearings are considered to be rigid so that, together with the rigid shafts, shaft–gear interfaces and gear blanks, they allow the gears to rotate only in torsional direction about their axes of rotation. (5) Gear mesh damping values are assumed to be constant (time-invariant) and not subject to gear backlash non-linearity. (6) Gears are assumed to be precise with no tooth-to-tooth variations and gear blank errors so that the motion transmission error excitation can be described by the gear mesh (tooth pass) frequency and its higher harmonics. This assumption also ensures that the gear backlash magnitudes remain constant.

In Fig. 1, each gear of polar mass moment of inertia I_i and base radius r_i is allowed to vibrate in torsional direction by $\bar{\theta}_i$, $(i = 1-4)$. Here, $\bar{\theta}_i$ represents the vibrations of gear i about its nominal rigid-body rotation $\Omega_i \bar{t}$, where Ω_i is the rotational speed in radians per second and $\bar{t}$ is real time in seconds. An over bar denotes that this parameter is dimensional. Gear mesh stiffnesses $k_1(\bar{t})$ and $k_2(\bar{t})$ represent gear mesh flexibilities of the first and second gear meshes. The gear mesh damping values are denoted by c_1 and c_2. These stiffness and damping elements were applied at respective gear meshes in the direction of the gear mesh line of action and displacement excitations $e_1(\bar{t})$ and $e_2(\bar{t})$ are connected in series to the stiffness and damping elements as shown in Fig. 1. Similar to the sdof model presented earlier, gear backlash non-linearities are introduced here as piecewise linear "dead-zone" type clearance functions $\bar{g}_1$ and $\bar{g}_2$ of amounts $2\bar{b}_1$ and $2\bar{b}_2$, respectively.

2.2. Equations of motion and non-dimensionalization

Since the shafts are assumed rigid both torsionally and in bending, the rotational displacements of gears 2 and 3 are equal, $\bar{\theta}_2(\bar{t}) = \bar{\theta}_3(\bar{t})$. Accordingly, the model shown in Fig. 1 can be represented by three degrees of freedom with coordinates $\bar{\theta}_1(\bar{t})$, $\bar{\theta}_2(\bar{t})$ and $\bar{\theta}_3(\bar{t})$, and the polar mass

moment of inertia associated with $\bar{\theta}_2(\bar{t})$ becomes $I_{23} = I_2 + I_3$. Equations of motion of this system can be obtained as

$$I_1\ddot{\bar{\theta}}_1(\bar{t}) + r_1c_1\left[r_1\dot{\bar{\theta}}_1(\bar{t}) + r_2\dot{\bar{\theta}}_2(\bar{t}) + \dot{\bar{e}}_1(\bar{t})\right] + r_1k_1(\bar{t})g_1(\bar{t}) = T_1(\bar{t}), \tag{1a}$$

$$I_{23}\ddot{\bar{\theta}}_2(\bar{t}) + r_2c_1\left[r_1\dot{\bar{\theta}}_1(\bar{t}) + r_2\dot{\bar{\theta}}_2(\bar{t}) + \dot{\bar{e}}_1(\bar{t})\right] + r_2k_1(\bar{t})\bar{g}_1(\bar{t}) + r_3c_2\left[r_3\dot{\bar{\theta}}_2(\bar{t}) + r_4\dot{\bar{\theta}}_4(\bar{t}) + \dot{\bar{e}}_2(\bar{t})\right] + r_3k_2(\bar{t})\bar{g}_2(\bar{t}) = 0, \tag{1b}$$

$$I_4\ddot{\bar{\theta}}_4(\bar{t}) + r_4c_2\left[r_3\dot{\bar{\theta}}_2(\bar{t}) + r_4\dot{\bar{\theta}}_4(\bar{t}) + \dot{\bar{e}}_2(\bar{t})\right] + r_4k_2(\bar{t})\bar{g}_2(\bar{t}) = T_4(\bar{t}), \tag{1c}$$

where $\bar{g}_1$ and $\bar{g}_2$ are non-linear type clearance functions defined mathematically as

$$\bar{g}_1 = \begin{cases} [r_1\bar{\theta}_1(\bar{t}) + r_2\bar{\theta}_2(\bar{t}) + \bar{e}_1(\bar{t})] - \bar{b}_1, & [r_1\bar{\theta}_1(\bar{t}) + r_2\bar{\theta}_2(\bar{t}) + \bar{e}_1(\bar{t})] > \bar{b}_1, \\ 0, & \left|r_1\bar{\theta}_1(\bar{t}) + r_2\bar{\theta}_2(\bar{t}) + \bar{e}_1(\bar{t})\right| \leqslant \bar{b}_1, \\ [r_1\bar{\theta}_1(\bar{t}) + r_2\bar{\theta}_2(\bar{t}) + \bar{e}_1(\bar{t})] + \bar{b}_1, & [r_1\bar{\theta}_1(\bar{t}) + r_2\bar{\theta}_2(\bar{t}) + \bar{e}_1(\bar{t})] < -\bar{b}_1, \end{cases} \tag{2a}$$

$$\bar{g}_2 = \begin{cases} [r_3\bar{\theta}_2(\bar{t}) + r_4\bar{\theta}_4(\bar{t}) + \bar{e}_2(\bar{t})] - \bar{b}_2, & [r_3\bar{\theta}_2(\bar{t}) + r_4\bar{\theta}_4(\bar{t}) + \bar{e}_2(\bar{t})] > \bar{b}_2, \\ 0, & \left|r_3\bar{\theta}_2(\bar{t}) + r_4\bar{\theta}_4(\bar{t}) + \bar{e}_2(\bar{t})\right| \leqslant \bar{b}_2, \\ [r_3\bar{\theta}_2(\bar{t}) + r_4\bar{\theta}_4(\bar{t}) + \bar{e}_2(\bar{t})] + \bar{b}_2, & [r_3\bar{\theta}_2(\bar{t}) + r_4\bar{\theta}_4(\bar{t}) + \bar{e}_2(\bar{t})] < -\bar{b}_2. \end{cases} \tag{2b}$$

Since the system is semi-definite with a rigid-body mode at zero natural frequency, the number of equations of motion can be reduced to two by defining the following two new coordinates:

$$\bar{p}_1(\bar{t}) = r_1\bar{\theta}_1(\bar{t}) + r_2\bar{\theta}_2(\bar{t}) + \bar{e}_1(\bar{t}), \quad \bar{p}_2(\bar{t}) = r_3\bar{\theta}_2(\bar{t}) + r_4\bar{\theta}_4(\bar{t}) + \bar{e}_2(\bar{t}). \tag{3a,b}$$

These new coordinates have physical significance since they represent the relative gear mesh displacements. Eqs. (1)–(3) are used to write

$$\ddot{\bar{p}}_1(\bar{t}) + c_1\left[\frac{r_1^2}{I_1} + \frac{r_2^2}{I_{23}}\right]\dot{\bar{p}}_1(\bar{t}) + c_2\left[\frac{r_2r_3}{I_{23}}\right]\dot{\bar{p}}_2(\bar{t}) + k_1(\bar{t})\left[\frac{r_1^2}{I_1} + \frac{r_2^2}{I_{23}}\right]\bar{g}_1(\bar{t}) + k_2(\bar{t})\left[\frac{r_2r_3}{I_{23}}\right]\bar{g}_2(\bar{t}) = \frac{r_1}{I_1}\bar{T}_1(\bar{t}) + \ddot{\bar{e}}_1(\bar{t}), \tag{4a}$$

$$\ddot{\bar{p}}_2(\bar{t}) + c_1\left[\frac{r_2r_3}{I_{23}}\right]\dot{\bar{p}}_1(\bar{t}) + c_2\left[\frac{r_3^2}{I_{23}} + \frac{r_4^2}{I_4}\right]\dot{\bar{p}}_2(\bar{t}) + \left[\frac{r_2r_3}{I_{23}}\right]k_1(\bar{t})\bar{g}_1(\bar{t}) + k_2(\bar{t})\left[\frac{r_3^2}{I_{23}} + \frac{r_4^2}{I_4}\right]\bar{g}_2(\bar{t}) = \frac{r_4}{I_4}\bar{T}_4(\bar{t}) + \ddot{\bar{e}}_2(\bar{t}). \tag{4b}$$

Define the following parameters:

$$m_1 = \frac{I_1I_{23}}{r_1^2I_{23} + I_1r_2^2}, \quad m_2 = \frac{I_{23}}{r_2r_3}, \quad m_3 = \frac{I_4I_{23}}{r_4^2I_{23} + I_4r_3^2}, \tag{5a–c}$$

$$\kappa_1(\bar{t}) = \frac{k_1(\bar{t})}{k_{1m}}, \quad \kappa_2(\bar{t}) = \frac{k_2(\bar{t})}{k_{2m}}, \tag{5a,b}$$

$$\bar{\omega}_{11}^2 = \frac{k_{1m}}{m_1}, \quad \bar{\omega}_{12}^2 = \frac{k_{2m}}{m_2}, \quad \bar{\omega}_{21}^2 = \frac{k_{1m}}{m_2}, \quad \bar{\omega}_{22}^2 = \frac{k_{2m}}{m_3}, \tag{5c–f}$$

$$\zeta_{11} = \frac{c_1}{2m_1\bar{\omega}_{11}}, \quad \zeta_{12} = \frac{c_2}{2m_2\bar{\omega}_{12}}, \quad \zeta_{21} = \frac{c_1}{2m_2\bar{\omega}_{21}}, \quad \zeta_{22} = \frac{c_2}{2m_3\bar{\omega}_{22}}, \tag{5g–j}$$

where k_{1m} and k_{2m} are the mean components of $k_1(t)$ and $k_2(t)$, respectively, $\bar{\omega}_{ij}$ $(i,j=1,2)$ are characteristic frequencies, and ζ_{ij} $(i,j=1,2)$ define the damping of the system. Further, a dimensionless time parameter is obtained by setting $t=\bar{t}\omega_c$, where ω_c is the characteristic frequency. Also employing a characteristic length b_c, dimensionless displacements are defined as $p_i(\bar{t})=\bar{p}_i(\bar{t})/b_c$, $e_i(\bar{t})=\bar{e}_i(\bar{t})/b_c$, and $b_i=\bar{b}_i/b_c$ $(i=1,2)$. Using these dimensionless parameters and letting $\omega_{ij}=\bar{\omega}_{ij}/\omega_c$ $(i,j=1,2)$, the following dimensionless equations of motion are obtained:

$$\begin{Bmatrix} \ddot{p}_1(t) \\ \ddot{p}_2(t) \end{Bmatrix} + 2\begin{bmatrix} \zeta_{11}\omega_{11} & \zeta_{12}\omega_{12} \\ \zeta_{21}\omega_{21} & \zeta_{22}\omega_{22} \end{bmatrix} \begin{Bmatrix} \dot{p}_1(t) \\ \dot{p}_2(t) \end{Bmatrix} + \begin{bmatrix} \omega_{11}^2\kappa_1(t) & \omega_{12}^2\kappa_2(t) \\ \omega_{21}^2\kappa_1(t) & \omega_{22}^2\kappa_2(t) \end{bmatrix} \begin{Bmatrix} g_1(t) \\ g_2(t) \end{Bmatrix} = \begin{Bmatrix} f_1(t) \\ f_2(t) \end{Bmatrix}, \tag{6a}$$

where

$$g_i(t) = \begin{cases} p_i(t) - b_i, & p_i(t) > b_i, \\ 0, & |p_i(t)| \leqslant b_i \\ p_i(t) + b_i, & p_i(t) < -b_i, \end{cases}, \quad i=1,2, \tag{6b}$$

and the forces caused by external sources at the gear mesh interface are written as

$$f_1(t) = \frac{r_1\bar{T}_1(t)}{I_1\omega_c^2 b_c} + \ddot{e}_1(t), \quad f_2(t) = \frac{r_4\bar{T}_4(t)}{I_4\omega_c^2 b_c} + \ddot{e}_2(t). \tag{6c}$$

3. Multi-term harmonic balance solution for period-1 motions

The multi-term HBM is based on the assumption that both external excitations and the time-varying coefficients are periodic. If functions $\kappa_i(t)$ and $f_i(t)$ in Eq. (6a) are both periodic in time, then the steady-state solutions $p_i(t)$ must also be periodic. This also implies that $g_i(t)$ can also be described periodically. Following a multi-term harmonic balance procedure that was applied to sdof nonlinear time-varying systems successfully [4,5,22], one writes $\kappa_i(t)$ and $f_i(t)$ in Fourier series form as

$$\kappa_1(t) = 1 + \sum_{h=1}^{K}\left[\kappa_{2h}^{(1)}\cos(h\Lambda t) + \kappa_{2h+1}^{(1)}\sin(h\Lambda t)\right], \tag{7a}$$

$$\kappa_2(t) = 1 + \sum_{h=1}^{K}\left[\kappa_{2h}^{(2)}\cos(hn\Lambda t) + \kappa_{2h+1}^{(2)}\sin(hn\Lambda t)\right], \tag{7b}$$

$$f_1(t) = f_1^{(1)} + \sum_{\ell=1}^{L}\left[f_{2\ell}^{(1)}\cos(\ell\Lambda t) + f_{2\ell+1}^{(1)}\sin(\ell\Lambda t)\right], \tag{8a}$$

$$f_2(t) = f_1^{(2)} + \sum_{\ell=1}^{L}\left[f_{2\ell}^{(2)}\cos(\ell\Lambda t) + f_{2\ell+1}^{(2)}\sin(\ell\Lambda t)\right]. \tag{8b}$$

Here, $\Lambda_1 = \Lambda$ and $\Lambda_2 = n\Lambda$ are the fundamental frequencies of the stiffness of the first and second gear meshes, respectively, where $\Lambda = \Omega_1/\omega_c$ is the dimensionless gear mesh frequency, and the multiplier n can be any real number as it defines the ratio of the number of teeth of gears 2 and 3 in Fig. 1, $n = Z_2/Z_3$.

Given the periodic excitations of Eqs. (7) and (8), the harmonic balance procedure requires that the steady-state response be periodic as well. Accordingly, one can describe $p_1(t)$ and $p_2(t)$ in Fourier series form as

$$p_1(t) = u_1^{(1)} + \sum_{r=1}^{R}\left[u_{2r}^{(1)}\cos(r\Lambda t) + u_{2r+1}^{(1)}\sin(r\Lambda t)\right], \tag{9a}$$

$$p_2(t) = u_1^{(2)} + \sum_{r=1}^{R}\left[u_{2r}^{(2)}\cos(rn\Lambda t) + u_{2r+1}^{(2)}\sin(rn\Lambda t)\right], \tag{9b}$$

where $u_1^{(1)}, u_{2r}^{(1)}, u_{2r+1}^{(1)}, u_1^{(2)}, u_{2r}^{(2)}, u_{2r+1}^{(2)}$ $(r = 1-R)$ are unknown coefficients of the assumed solution [22]. In order to preserve the harmonic balance in Eq. (6a), the non-linear functions $g_1(t)$ and $g_2(t)$ defined in Eq. (6b) must be assumed to be periodic as well at the same harmonic orders as the excitations:

$$g_1(t) = v_1^{(1)} + \sum_{r=1}^{R}\left[v_{2r}^{(1)}\cos(r\Lambda t) + v_{2r+1}^{(1)}\sin(r\Lambda t)\right], \tag{10a}$$

$$g_2(t) = v_1^{(2)} + \sum_{r=1}^{R}\left[v_{2r}^{(2)}\cos(rn\Lambda t) + v_{2r+1}^{(2)}\sin(rn\Lambda t)\right]. \tag{10b}$$

Here $v_1^{(i)}$, $v_{2r}^{(i)}$ and $v_{2r+1}^{(i)}$ $(r = 1-R$ and $i = 1, 2)$ are the so-called describing functions [4,22] that must be determined before the unknown response parameters can be found. Before substituting Eqs. (7–10) into Eq. (6a), the last mathematical transformation is introduced in the form $\theta = \Lambda t$ where

$$\frac{\mathrm{d}p_1}{\mathrm{d}t} = \sum_{r=1}^{R}\left[-\Lambda r u_{2r}^{(1)}\sin(r\theta) + \Lambda r u_{2r+1}^{(1)}\cos(r\theta)\right], \tag{11a}$$

$$\frac{\mathrm{d}^2p_1}{\mathrm{d}t^2} = \sum_{r=1}^{R}\left[-(\Lambda r)^2 u_{2r}^{(1)}\cos(r\theta) - (\Lambda r)^2 u_{2r+1}^{(1)}\sin(r\theta)\right], \tag{11b}$$

$$\frac{\mathrm{d}p_2}{\mathrm{d}t} = \sum_{r=1}^{R}\left[-\Lambda rn u_{2r}^{(2)}\sin(rn\theta) + \Lambda rn u_{2r+1}^{(2)}\cos(rn\theta)\right], \tag{11c}$$

$$\frac{\mathrm{d}^2p_2}{\mathrm{d}t^2} = \sum_{r=1}^{R}\left[-(\Lambda rn)^2 u_{2r}^{(2)}\cos(rn\theta) - (\Lambda rn)^2 u_{2r+1}^{(2)}\sin(rn\theta)\right]. \tag{11d}$$

With this, products $\kappa_i(t)g_i(t)$ in Eq. (6a) can be evaluated as

$$\begin{aligned}\kappa_1(t)g_1(t) = {} & v_1^{(1)} + v_1^{(1)}\sum_{h=1}^{H}\left[\kappa_{2h}^{(1)}\cos(h\theta) + \kappa_{2h+1}^{(1)}\sin(h\theta)\right] \\ & + \sum_{r=1}^{R}\left[v_{2r}^{(1)}\cos(r\theta) + v_{2r+1}^{(1)}\sin(r\theta)\right] + \frac{1}{2}\sum_{r=1}^{R}\sum_{h=1}^{H}\Big\{\kappa_{2h}^{(1)}v_{2r}^{(1)}[\cos(r-h)\theta + \cos(r+h)\theta] \\ & + \kappa_{2h+1}^{(1)}v_{2r+1}^{(1)}[\cos(r-h)\theta - \cos(r+h)\theta] + \kappa_{2h}^{(1)}v_{2r+1}^{(1)}[\sin(r-h)\theta + \sin(r+h)\theta] \\ & + \kappa_{2h+1}^{(1)}v_{2r}^{(1)}[-\sin(r-h)\theta + \sin(r+h)\theta]\Big\}, \end{aligned} \tag{12a}$$

$$\begin{aligned}\kappa_2(t)g_2(t) = {} & v_1^{(2)} + v_1^{(2)}\sum_{h=1}^{H}\left[\kappa_{2h}^{(2)}\cos(hn\theta) + \kappa_{2h+1}^{(2)}\sin(hn\theta)\right] \\ & + \sum_{r=1}^{R}\left[v_{2r}^{(2)}\cos(rn\theta) + v_{2r+1}^{(2)}\sin(rn\theta)\right] + \frac{1}{2}\sum_{r=1}^{R}\sum_{h=1}^{H}\Big\{\kappa_{2h}^{(2)}v_{2r}^{(2)}[\cos n(r-h)\theta + \cos n(r+h)\theta] \\ & + \kappa_{2h+1}^{(2)}v_{2r+1}^{(2)}[\cos n(r-h)\theta - \cos n(r+h)\theta] + \kappa_{2h+1}^{(2)}v_{2r+1}^{(2)}[\cos n(r-h)\theta - \cos n(r+h)\theta] \\ & + \kappa_{2h+1}^{(2)}v_{2r}^{(2)}[-\sin n(r-h)\theta + \sin n(r+h)\theta]\Big\}. \end{aligned} \tag{12b}$$

Substituting Eqs. (8), (9) (11) and (12) into Eq. (6a), neglecting higher-order terms and equating the coefficients of like harmonic terms, a set of $(4R + 2)$ non-linear algebraic equations are obtained, which can be written in vector form as

$$\mathbf{S}(\mathbf{u}, \mathbf{v}, \Lambda) = \mathbf{0}, \tag{13}$$

where vectors $\mathbf{u}$, $\mathbf{v}$ and $\mathbf{S}$ have dimension $(4R + 2)$ and the elements of $\mathbf{S}$ are given as ($r \in [1, R]$)

$$\begin{aligned} S_1^{(1)} = {} & \omega_{11}^2\left\{v_1^{(1)} + \tfrac{1}{2}\sum_{i=1}^{R}(v_{2i}^{(1)}\kappa_{2i}^{(1)} + v_{2i+1}^{(1)}\kappa_{2i+1}^{(1)})\right\} \\ & + \omega_{12}^2\left\{v_1^{(2)} + \tfrac{1}{2}\sum_{i=1}^{R}(v_{2i}^{(2)}\kappa_{2i}^{(2)} + v_{2i+1}^{(2)}\kappa_{2i+1}^{(2)})\right\} - f_1^{(1)}, \end{aligned} \tag{14a}$$

$$\begin{aligned} S_{2r}^{(1)} = {} & -(\Lambda r)^2 u_{2r}^{(1)} + 2\zeta_{11}\omega_{11}\Lambda r u_{2r+1}^{(1)} + 2\zeta_{12}\omega_{12}\Lambda r u_{2(r/n)+1}^{(2)} \\ & + \omega_{11}^2\left\{\left(v_{2r}^{(1)} + v_1^{(1)}\kappa_{2r}^{(1)}\right) + \tfrac{1}{2}\sum_{i=1}^{R}\left(\kappa_{2i+1}^{(1)}\psi_1^{(1)} + \kappa_{2i}^{(1)}\psi_2^{(1)}\right)\right\} \\ & + \omega_{12}^2\left\{\left(v_{2r/n}^{(2)} + v_1^{(2)}\kappa_{2r/n}^{(2)}\right) + \tfrac{1}{2}\sum_{i=1}^{R}\left(\kappa_{2i+1}^{(2)}\psi_1^{(2)} + \psi_2^{(2)}\kappa_{2i}^{(2)}\right)\right\} - f_{2r}^{(1)}, \end{aligned} \tag{14b}$$

$$S_{2r+1}^{(1)} = -(\Lambda r)^2 u_{2r+1}^{(1)} - 2\zeta_{11}\omega_{11}\Lambda r\, u_{2r}^{(1)} - 2\zeta_{12}\omega_{12}\Lambda r\, u_{2r/n}^{(2)} + \omega_{11}^2\left\{\left(v_{2r+1}^{(1)} + v_1^{(1)}\kappa_{2r+1}^{(1)}\right) + \tfrac{1}{2}\sum_{i=1}^{R}\left(\kappa_{2i}^{(1)}\psi_3^{(1)} + \kappa_{2i+1}^{(1)}\psi_4^{(1)}\right)\right\} + \omega_{12}^2\left\{\left(v_{2(r/n)+1}^{(2)} + v_1^{(2)}\kappa_{(2r/n)+1}^{(2)}\right) + \tfrac{1}{2}\sum_{i=1}^{R}\left(\kappa_{2i}^{(2)}\psi_3^{(2)} + \kappa_{2i+1}^{(2)}\psi_4^{(2)}\right)\right\} - f_{2r+1}^{(1)}, \tag{14c}$$

$$S_1^{(2)} = \omega_{21}^2\left\{v_1^{(1)} + \tfrac{1}{2}\sum_{i=1}^{R}\left(v_{2i}^{(1)}\kappa_{2i}^{(1)} + v_{2i+1}^{(1)}\kappa_{2i+1}^{(1)}\right)\right\} + \omega_{22}^2\left\{v_1^{(2)} + \tfrac{1}{2}\sum_{i=1}^{R}\left(v_{2i}^{(2)}\kappa_{2i}^{(2)} + v_{2i+1}^{(2)}\kappa_{2i+1}^{(2)}\right)\right\} - f_1^{(2)}, \tag{14d}$$

$$S_{2r}^{(2)} = -(\Lambda r)^2 u_{2r/n}^{(2)} + 2\zeta_{21}\omega_{21}\Lambda r\, u_{2r+1}^{(1)} + 2\zeta_{22}\omega_{22}\Lambda r\, u_{2(r/n)+1}^{(2)} + \omega_{21}^2\left\{\left(v_{2r}^{(1)} + v_1^{(1)}\kappa_{2r}^{(1)}\right) + \frac{1}{2}\sum_{i=1}^{R}\left(\kappa_{2i}^{(1)}\psi_2^{(1)} + \kappa_{2i+1}^{(1)}\psi_1^{(1)}\right)\right\} + \omega_{22}^2\left\{\left(v_{2r/n}^{(2)} + v_1^{(2)}\kappa_{2r/n}^{(2)}\right) + \tfrac{1}{2}\sum_{i=1}^{R}\left(\kappa_{2i+1}^{(2)}\psi_1^{(2)} + \kappa_{2i}^{(2)}\psi_2^{(2)}\right)\right\} - f_{2r}^{(2)}, \tag{14e}$$

$$S_{2r+1}^{(2)} = -(\Lambda r)^2 u_{(2r/n)+1}^{(2)} - 2\zeta_{21}\omega_{21}\Lambda r\, u_{2r}^{(1)} - 2\zeta_{22}\omega_{22}\Lambda r\, u_{2r/n}^{(2)} + \omega_{21}^2\left\{\left(v_1^{(1)}\kappa_{2r+1}^{(1)} + v_{2r+1}^{(1)}\right) + \tfrac{1}{2}\sum_{i=1}^{R}\left(\kappa_{2i}^{(1)}\psi_3^{(1)} + \kappa_{2i+1}^{(1)}\psi_4^{(1)}\right)\right\} + \omega_{22}^2\left\{\left(v_1^{(2)}\kappa_{2(r/n)+1}^{(2)} + v_{2(r/n)+1}^{(2)}\right) + \tfrac{1}{2}\sum_{r=1}^{R}\left(\kappa_{2i}^{(2)}\psi_3^{(2)} + \kappa_{2i+1}^{(2)}\psi_4^{(2)}\right)\right\} - f_{2r+1}^{(2)}, \tag{14f}$$

where

$$\psi_1^{(1)} = v_{2(i-r)+1}^{(1)} + v_{2(i+r)+1}^{(1)} - v_{2(r-i)+1}^{(1)}, \tag{14g}$$

$$\psi_2^{(1)} = v_{2(i-r)}^{(1)} + v_{2(i+r)}^{(1)} + v_{2(r-i)}^{(1)}, \tag{14h}$$

$$\psi_3^{(1)} = -v_{2(i-r)+1}^{(1)} + v_{2(i+r)+1}^{(1)} + v_{2(r-i)+1}^{(1)}, \tag{14i}$$

$$\psi_4^{(1)} = v_{2(i-r)}^{(1)} - v_{2(i+r)}^{(1)} + v_{2(r-i)}^{(1)}, \tag{14j}$$

$$\psi_1^{(2)} = v_{2(i-r/n)+1}^{(2)} + v_{2(i+r/n)+1}^{(2)} - v_{2(r/n-i)+1}^{(2)} \tag{14k}$$

$$\psi_2^{(2)} = v_{2(i-r/n)}^{(2)} + v_{2(i+r/n)}^{(2)} + v_{2(r/n-i)}^{(2)}, \tag{14l}$$

$$\psi_3^{(2)} = -v_{2(i-r/n)+1}^{(2)} + v_{2(i+r/n)+1}^{(2)} + \kappa_{2(r/n-i)+1}^{(2)}, \tag{14m}$$

$$\psi_4^{(2)} = v_{2(i-r/n)}^{(2)} - v_{2(i+r/n)}^{(2)} + v_{2(r/n-i)}^{(2)}. \tag{14n}$$

In later steps, the selection of Λ as a control parameter to solve for the elements of $\mathbf{u}$ using the Newton–Raphson iteration method poses difficulties. As the solution approaches (singular)

bifurcation points, the determinant of the Jacobian matrix also approaches zero. This can be avoided by switching to another unknown as the control parameter, leaving the dimensionless frequency Λ and the other elements of the solution vector $\mathbf{u}$ as unknowns to be determined. In order to implement this, $\mathbf{u}$ is expanded to $\mathbf{U} = [\mathbf{u}^{\mathrm{T}}, u_{4R+3}]^{\mathrm{T}}$ where $u_{4R+3} = \Lambda$. Accordingly, the following dummy equation is added to Eq. (14a–f):

$$S_{4R+3} = u_j^{(\ell)} - u^*, \tag{14o}$$

where the values of the indices $j \in [1, 2R+1]$ and $\ell = 1\, or\, 2$ define which element other than the frequency ratio Λ is chosen as a control parameter, and u^* is a numerical value assigned to the control parameter, $u_j^{(\ell)} = u.^*$

Before the above equations can be solved for the unknown response coefficients $u_i^{(j)}$ ($j = 1, 2$, $i = 1$ to $2R+1$) and u_{4R+3}, the coefficients of the nonlinear displacement functions $v_i^{(j)}$ must be represented in terms of $u_i^{(j)}$. This is done by making use of the discrete Fourier transforms [4,22]. The values of the $p_i(t)$ and $g_i(t)$ at the discrete time $t = q\rho$ (where $q \in [0, Q-1]$) are

$$p_{1q} = u_1^{(1)} + \sum_{r=1}^{R}\left[u_{2r}^{(1)} \cos\left(\frac{2\pi rq}{Q}\right) + u_{2r+1}^{(1)} \sin\left(\frac{2\pi rq}{Q}\right)\right], \tag{15a}$$

$$p_{2q} = u_1^{(2)} + \sum_{r=1}^{R}\left[u_{2r}^{(2)} cos\left(\frac{2\pi rnq}{Q}\right) + u_{2r+1}^{(2)} \sin\left(\frac{2\pi rnq}{Q}\right)\right], \tag{15b}$$

and

$$g_{iq} = \begin{cases} p_{iq}(t) - b_i, & p_{iq}(t) > b_i, \\ 0, & |p_{iq}(t)| \leqslant b_i, \\ p_{iq}(t) + b_i, & p_{iq}(t) < -b_i, \end{cases} \qquad i = 1, 2. \tag{15c}$$

Here $\rho = 2\pi/(Q\Lambda)$ where Q is the total number of the discrete points and $Q \geqslant 2R$ in order to prevent any aliasing errors [23].

Given above discretization, the coefficients of $g_1(t)$ and $g_2(t)$ can be determined by using the Inverse Fourier transforms such that ($r \in [1, R]$)

$$v_1^{(1)} = \frac{1}{Q}\sum_{q=0}^{Q-1} g_{1q}, \quad v_1^{(2)} = \frac{1}{Q}\sum_{q=0}^{Q-1} g_{2q}, \tag{16a,b}$$

$$v_{2r}^{(1)} = \frac{2}{Q}\sum_{q=0}^{Q-1} g_{1q} \cos\left(\frac{2\pi rq}{Q}\right), \quad v_{2r}^{(2)} = \frac{2}{Q}\sum_{q=0}^{Q-1} g_{2q} cos\left(\frac{2\pi rnq}{Q}\right), \tag{16c,d}$$

$$v_{2r+1}^{(1)} = \frac{2}{Q}\sum_{q=0}^{Q-1} g_{1q} \sin\left(\frac{2\pi rq}{Q}\right), \quad v_{2r+1}^{(2)} = \frac{2}{Q}\sum_{q=0}^{Q-1} g_{2q} \sin\left(\frac{2\pi rnq}{Q}\right). \tag{16e,f}$$

The above values of $v_i^{(j)}$ are substituted into Eqs. (14a–f, 14o) to obtain $(4R+3)$ non-linear algebraic equations with the same number of unknowns given by the vector

$$\mathbf{U} = \left[u_1^{(1)}, u_2^{(1)}, \ldots, u_{2R}^{(1)}, u_{2R+1}^{(1)}, u_1^{(2)}, u_2^{(2)}, \ldots, u_{2R}^{(2)}, u_{2R+1}^{(2)}, u_{4R+3}\right]^{\mathrm{T}}.$$

The last step in the solution methodology becomes the application of a Newton–Raphson iteration procedure. The recurrence formula for this iteration procedure can be written as

$$\mathbf{U}^{(m)} = \mathbf{U}^{(m-1)} - \left(\mathbf{J}^{-1}\right)^{(m-1)}\mathbf{S}^{(m-1)}, \tag{17}$$

where $\mathbf{U}^{(\mathrm{m}-1)}$ and $\mathbf{U}^{(\mathrm{m})}$ are the previous and the current iteration values of the vector $\mathbf{U}$ respectively, and $\left(\mathbf{J}^{-1}\right)^{(m-1)}$ is the inverse of the Jacobian matrix of the vector $\mathbf{S}$ estimated at the previous point $(m-1)$. The solution procedure starts with an initial solution guess $\mathbf{U}^{(0)}$ to evaluate $\mathbf{U}^{(1)}$. The value of the control parameter is set to u^*. The vector $\mathbf{U}^{(1)}$ in turn is used as an initial guess for the next iteration until the steady state solution $\mathbf{U}^{(m)}$ converges within a certain predefined error limit. The control parameter is set to the next value of interest by increasing or decreasing u^* until a bifurcation point impedes continuation. Then another unknown is adapted as the new control parameter. The individual elements of the Jacobian matrix are determined by evaluating partial derivatives $\partial S_i^{(\ell)}/\partial u_j^{(\ell)}$ and $\partial S_{4R+3}/\partial \Lambda$, where $\Lambda = u_{4R+3}$, $i \in [1, R]$, $j \in [1, 2R+1]$ and $\ell = 1, 2$ [4,5].

The stability of period-1 steady state solutions is determined by using the Floquet theory [24]. For this purpose, the governing equations of motion are written in state space form $\dot{\mathbf{P}}(t) = \mathbf{F}(\mathbf{P}(t), \hat{\lambda})$, where $\mathbf{P}(t) = \mathbf{P}(t+jT) = [p_1(t), p_2(t), \dot{p}_1(t), \dot{p}_2(t),]^{\mathrm{T}}$ $(j = 1, 2, \ldots)$ is a periodic solution of fundamental period T and $\hat{\lambda}$ is a control parameter, which is actually one of the system parameters $(\zeta_{ij}, \omega_{ij}, \kappa_{ij}, b_i)$. Application of Floquet theory yields an homogeneous matrix equation $\dot{\mathbf{Z}} = \mathbf{W}\mathbf{Z}$ given initial condition $\mathbf{Z}(0) = \mathbf{I}_4$, where $\mathbf{I}_4$ is an identity matrix of dimension 4. Solution of this equation gives the Monodromy matrix $\mathbf{M} = \mathbf{Z}(T)$ whose eigenvalues determine the stability of the entire solution. Whenever the modulus of any of the four eigenvalues λ_i is greater than unity $|\lambda_i| > 1$, the solution is unstable. Contrary, if all $|\lambda_i| < 1$, the steady-state solution found by the HBM is stable.

4. Results and discussion

An example gear pair is considered here to determine the accuracy of the harmonic balance solutions by comparing to direct numerical integration results and to quantify the sensitivity of period-1 response to key system parameters including gear mesh stiffness amplitudes, gear mesh damping and static force (torque) transmitted. The dimensionless system parameters of this example gear train are also calculated by using the dimensional parameters listed in Table 1 and the relationships given in Section 3. In order to limit the parameter set, only the fundamental harmonics of the mesh stiffness functions $\kappa_1(t)$ and $\kappa_2(t)$ are considered in most cases. In other words, in Eq. (7), $K = 1$ and the mesh stiffness functions are harmonic. Similarly, external forcing functions are considered to be constant with no disturbances in the form of torque pulsations and kinematic gear transmission errors ($\bar{T}_1(\bar{t}) = \text{constant}$, $\bar{T}_4(\bar{t}) = \text{constant}$, $e_1(\bar{t}) = e_2(\bar{t}) = 0$),

Table 1
Dimensional parameters of the baseline example gear pair

Parameter	Gear 1	Gear 2	Gear 3	Gear 4
Base circle radius, m	0.10	0.05	0.10	0.05
Mass, kg	14.81	3.7	7.4	1.85
Inertia, kg m^2	0.074	0.0046	0.0375	0.0023
Mean mesh stiffness, N/m	$5(10)^8$		$2.5(10)^8$	
Mesh damping coefficient, N s/m	2721		1360	

resulting in constant $f_1(t)$ and $f_2(t)$ in Eq. (10). Initially, it is assumed that gears 2 and 3 have the same number of teeth, $n = Z_2/Z_3 = 1$.

4.1. Comparison to numerical integration results

Fig. 2 compares the period-1 harmonic balance (HBM) solution to the direct numerical integration (NI) results. Here, the analytical solutions were obtained by assuming a three-term solution ($R = 3$ in Eq. (9)). Dimensionless system parameters are $\zeta = 0.05$ where $\zeta = c_1/2\sqrt{k_{1m}m_{12}} = c_2/2\sqrt{k_{2m}m_{34}}$, $m_{12} = I_1I_2/(r_1^2I_2 + r_2^2I_1)$, $m_{34} = I_3I_4/(r_3^2I_4 + r_4^2I_3)$, $\kappa_2^{(1)} = \kappa_2^{(2)} = 0.3$ corresponding to a gear involute contact ratio value of 1.7 [25], and $f_1^{(2)} = 4f_1^{(1)} = 0.184$ corresponding to an input torque value of $T_1 = 100$ N m. A characteristic length of $b_c = 30\,\mu$m is considered with $b_1 = b_2 = 1$, which means that each gear mesh has 60 μm total backlash. The dimensional characteristic frequency $\omega_c = 9874$ rad/s corresponds to the $\bar{\omega}_{11}$ for the system parameters of Table 1. With this, the undamped natural frequencies of the corresponding linear system are $\omega_{n1} = 0.96$ and $\omega_{n2} = 1.86$. In Fig. 2, the vertical axes represent the root-mean-square (rms) values defined as $p_j^{(\mathrm{rms})} = \{\sum_{r=1}^{3}[A_r^{(j)}]^2\}^{1/2}$. Here $A_r^{(j)}$ is the amplitude of the rth harmonic of $p_j(t)$ that is defined as $A_r^{(j)} = \{[u_{2r}^{(j)}]^2 + [u_{2r+1}^{(j)}]^2\}^{1/2}$. In Fig. 2(a), $p_1^{(\mathrm{rms})}$ is plotted as a function of Λ. The thick solid lines represent stable HBM solutions, while thin lines are the unstable HBM solutions and square symbols represent the NI solutions. A very good agreement is observed between the two solution methods, as stable HBM solutions are almost identical to NI motions. The same is true for $p_2^{(\mathrm{rms})}$ as well, as shown in Fig. 2(b).

Focusing on Fig. 2, $p_1^{(\mathrm{rms})}$ and $p_2^{(\mathrm{rms})}$ forced response curves exhibits softening-type nonlinear behavior near primary resonance frequencies at $\Lambda \approx \omega_{n1} = 0.96$ and $\Lambda \approx \omega_{n2} = 1.86$. In case of $p_1^{(\mathrm{rms})}$, a sudden increase (jump up) in the rms amplitude is observed at $\Lambda = 0.836$ as Λ is increased. Similarly, a jump down at $\Lambda = 0.57$ occurs as Λ is reduced defining a band of Λ in which two stable solutions and one unstable solution coexist. This is in line with the dynamic behavior of a single spur gear pair reported earlier [4,5,19]. The $p_1^{(\mathrm{rms})}$ curve has another jump discontinuity near $\Lambda \approx \omega_{n2} = 1.86$ as well, while the jumps are not very drastic, suggesting that the first natural mode involves larger relative motions of the first gear mesh. On the other hand, $p_2^{(\mathrm{rms})}$ response in Fig. 2(b) exhibits a large jump discontinuity near the primary resonance of $\Lambda \approx \omega_{n2} = 1.86$ with jump-up and jump-down frequencies at $\Lambda = 1.53$ and 1.24, respectively. Meanwhile, the discontinuity near $\Lambda \approx \omega_{n1} = 0.96$ is not that significant suggesting that the second mode is associated with larger relative motions of the second gear mesh.

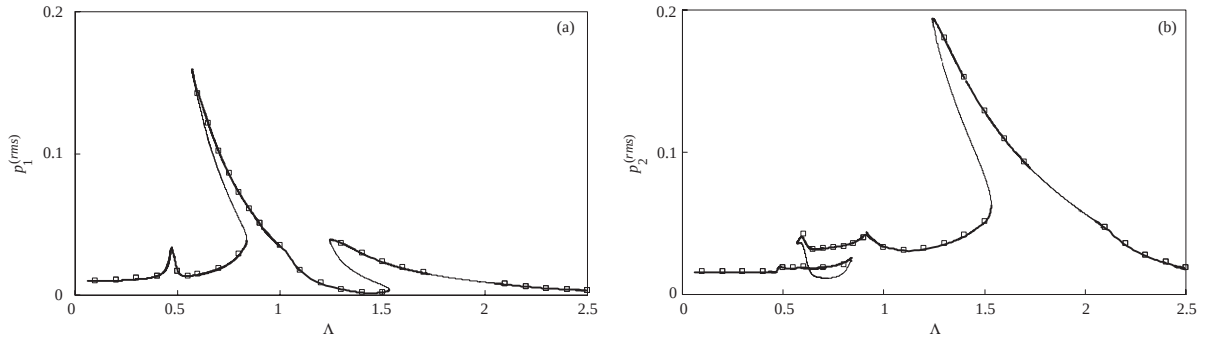

Fig. 2. Comparison of rms value of period-1 motions predicted by HBM and NI, for $R = 3$, $\zeta = 0.05$, $K = 1$, $\kappa_2^{(1)} = \kappa_2^{(2)} = 0.3$, $\omega_{n2} \approx 2\omega_{n1} = 1.86$, $f_1^{(2)} = 4f_1^{(1)} = 0.185$, $b_1 = b_2 = 1.0$ and $b_c = 30\,\mu m$ (—) Stable and (——) unstable HBM solution, and (□) NI solutions. (a) $p_1^{(rms)}$, (b) $p_2^{(rms)}$.

One other observation from Fig. 2 is that, while not very significant, super-harmonic resonance peaks also exist near $\Lambda \approx \frac{1}{2}\omega_{n1} = 0.48$ and $\Lambda \approx \frac{1}{2}\omega_{n1} = 0.93$. The first one is evident in Fig. 2(a) while the other one is identifiable in Fig. 2(b). These super-harmonic resonances appear when R is larger, and are not possible to detect if only a one-term harmonic solution ($R = 1$) is sought. It is also clear that double-sided impacts (DSI) are not observed here while the nonlinear motions are associated with the single-sided impacts (SSI). In physical terms, near the primary resonances, teeth on both gear meshes lose contact, yet since the vibration amplitudes are small compared to total backlash values, contacts at the backside of the teeth do not occur.

It is also clear in Fig. 2 that the period-1 motion looses its stability between $\Lambda = 1.71$ and 2.05. Within this region, there is no stable period-1 solution. This region of instability corresponds to the fundamental parametric resonance at $\Lambda \approx 2\omega_{n1}$. A similar unstable region can be expected near $\Lambda \approx 2\omega_{n2}$ as well. This is in agreement with the experimental data [2,5,19] on single gear pairs and LTV model predictions [16–18]. However, there are other stable period-n sub-harmonic motions dictating these ranges, preventing the gear train from exhibiting excessive vibration amplitudes. The prediction of such motions is beyond the scope of this study and is studied in another companion paper by these authors [21].

In Fig. 3(a) and (b), the mean amplitudes of $p_1(t)$ and $p_2(t)$ are plotted against Λ for the same case of Fig. 2. Obviously, if there were no tooth separations, the system would behave in a linear fashion and the values of $u_1^{(1)}$ and $u_1^{(2)}$ would remain constant as Λ varied. This is not the case in Fig. 3. The mean values remain constant for $\Lambda < 0.5$ as tooth separations are yet to occur. For $\Lambda > 0.5$, $u_1^{(1)}$ and $u_1^{(2)}$ vary significantly due to nonlinear behavior. It is also evident from Fig. 6 that HBM and NI solutions are again in very good agreement.

In Figs. 4 and 5, the harmonic amplitudes of $p_1(t)$ and $p_2(t)$ are shown for the same case of Fig. 2. Only the first three harmonic amplitudes $A_r^{(j)}$, $r = 1, 2, 3$ and $j = 1, 2$ are considered in these figures. It is noted in Fig. 4(a) and 5(a) that $A_1^{(j)}$ represent most of the motion especially near the primary resonance regions. This would indeed represent the total response if only a one-term HBM solution were sought, i.e. $R = 1$. Considering $R = 3$ results in the motion described in Fig. 2 with second and third harmonics $A_2^{(j)}$ and $A_3^{(j)}$ given in Figs. 4(b,c) and 5(b,c). It is noted in Figs. 4(b) and 5(c) that the super-harmonic resonances observed in Fig. 2 are caused by the higher harmonics of the response.

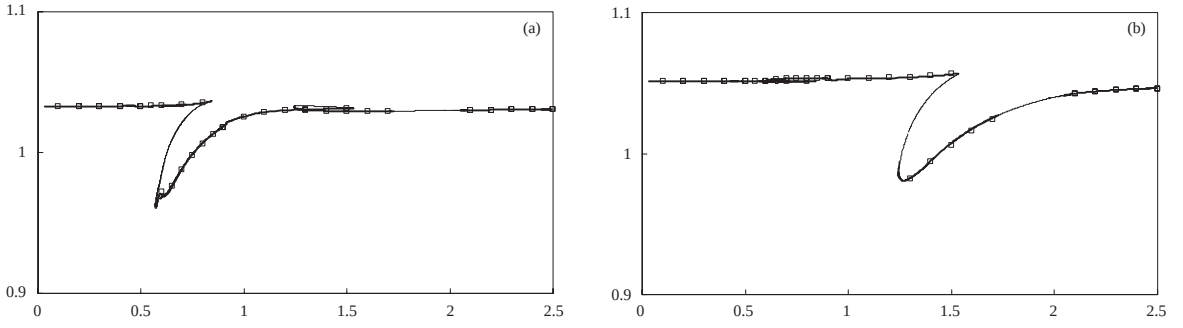

Fig. 3. Comparison of the mean components of $p_1(t)$ and $p_2(t)$ for $R = 3$, $\zeta = 0.05$, $K = 1$, $\kappa_2^{(1)} = \kappa_2^{(2)} = 0.3$, $\omega_{n2} \approx 2\omega_{n1} = 1.86, f_1^{(2)} = 4f_1^{(1)} = 0.185$, $b_1 = b_2 = 1.0$ and $b_c = 30\,\mu\text{m}$. (—) Stable and (——) unstable HBM solution, and (□) NI solutions. (a) $u_1^{(1)}$, (b) $u_1^{(2)}$.

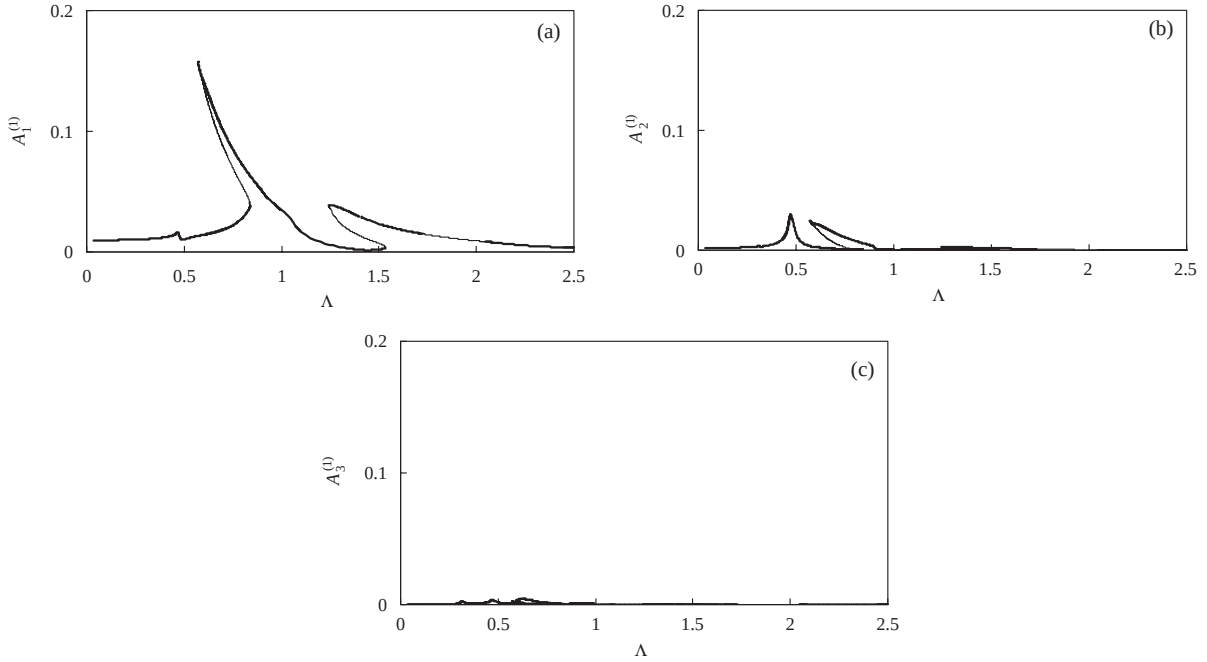

Fig. 4. The first three harmonic amplitudes of $p_1(t)$ for $R = 3$, $\zeta = 0.05$, $K = 1$, $\kappa_2^{(1)} = \kappa_2^{(2)} = 0.3$, $f_1^{(2)} = 4f_1^{(1)} = 0.185$, $b_1 = b_2 = 1.0$ and $b_c = 30\,\mu\text{m}$. (—) Stable and (——) unstable HBM solutions. (a) $A_1^{(1)}$, (b) $A_2^{(1)}$, and (c) $A_3^{(1)}$.

4.2. Parameter sensitivity studies

Influence of the mean force transmitted by the gear train on the steady-state period-1 response is shown in Fig. 6. Here the same system as Fig. 2 considered under torque values of $T = 50$, 100 and 150 N m. In agreement with previous observations on single gear pairs [4,5,19], increasing the mean force does not prevent tooth separations from occurring. With increasing mean force values $f_1^{(1)}$ and $f_1^{(2)}$, the shapes of the $p_1^{(\text{rms})}$ and $p_2^{(\text{rms})}$ curves remain the same, but the

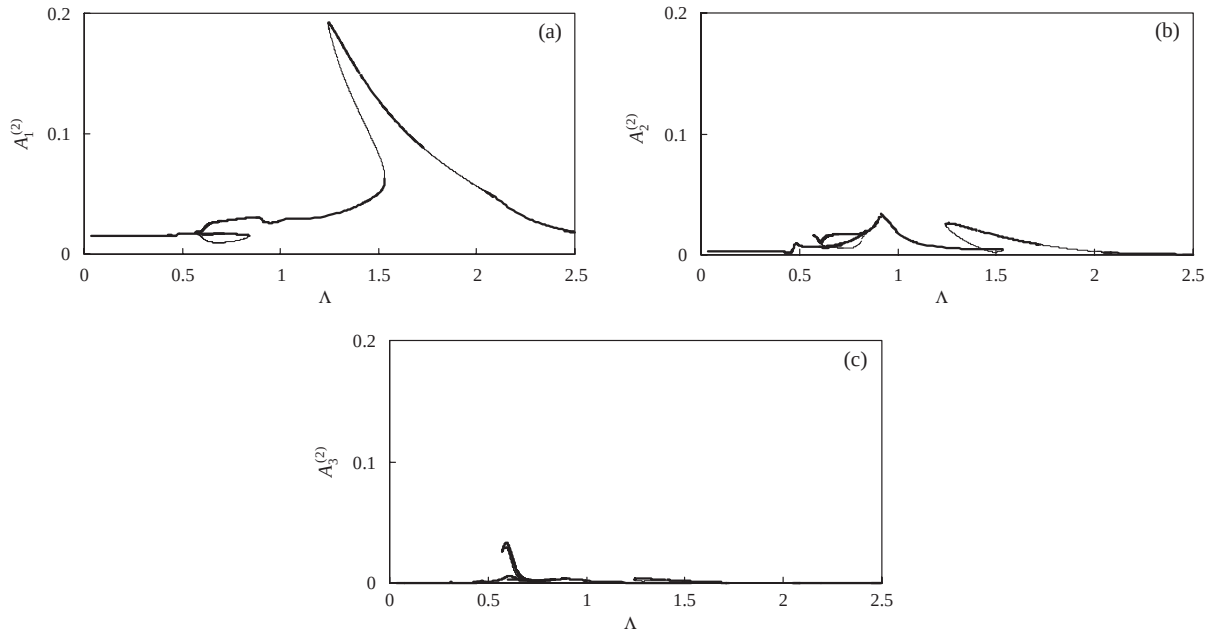

Fig. 5. The first three harmonic amplitudes of $p_2(t)$ for $R = 3$, $\zeta = 0.05$, $K = 1$, $\kappa_2^{(1)} = \kappa_2^{(2)} = 0.3$, $f_1^{(2)} = 4f_1^{(1)} = 0.185$, $b_1 = b_2 = 1.0$ and $b_c = 30\,\mu m$. (—) Stable and (——) unstable HBM solutions. (a) $A_1^{(2)}$, (b) $A_2^{(2)}$, and (c) $A_3^{(2)}$.

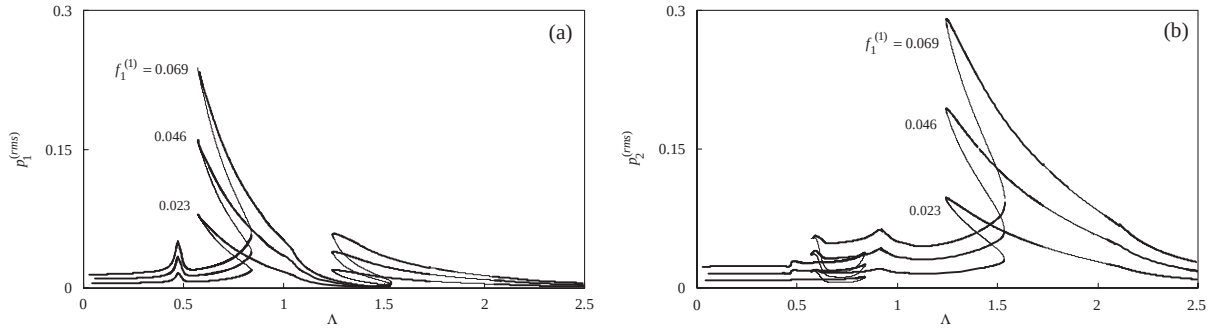

Fig. 6. Influence of the mean load on $p_j^{(rms)}$ for $R = 3$, $\zeta = 0.05$, $K = 1$, $\kappa_2^{(1)} = \kappa_2^{(2)} = 0.3$, $\omega_{n2} \approx 2\omega_{n1} = 1.86$, $f_1^{(2)} = 4f_1^{(1)}$, $b_1 = b_2 = 1$ and $b_c = 30\,\mu m$. (—) Stable and (——) unstable HBM solutions. (a) $p_1^{(rms)}$, (b) $p_2^{(rms)}$.

overall amplitudes are increased as shown in Fig. 6. The region of unstable period-1 motions also is not influenced by the values of $f_1^{(1)}$ and $f_1^{(2)}$.

In Fig. 7, the influence of the damping ratio on the rms response parameters are shown. Here, the backlash values are reduced to $b_1 = b_2 = \frac{1}{3}$ in order to increase the chance of obtaining DSI motions, especially when the system is very lightly damped. Three levels of damping, $\zeta =$ 0.1, 0.05 and 0.02, are considered in Fig. 7 to demonstrate that damping has a very significant influence on the dynamic response. When the system is damped heavily ($\zeta = 0.1$), the nonlinear behavior is almost negligible as the jump discontinuities and overall response amplitudes become

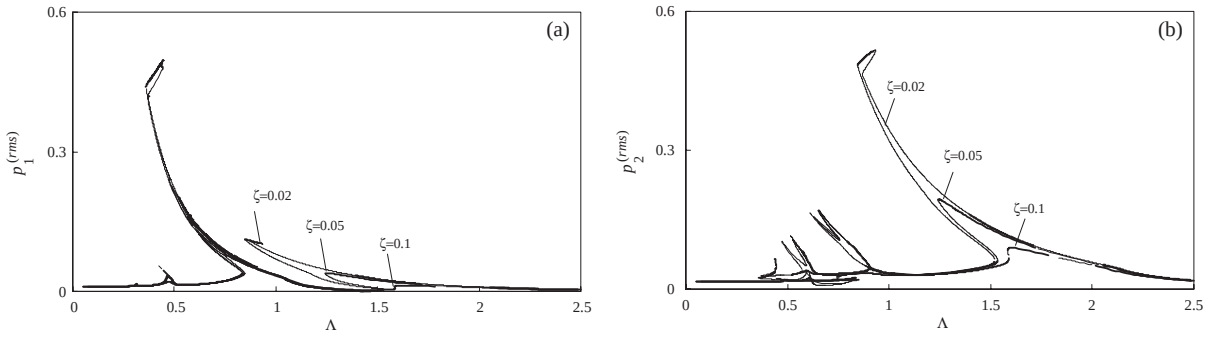

Fig. 7. Influence of the damping ratio on $p_j^{(\mathrm{rms})}$ for $R=3$, $\zeta=0.05$, $K=1$, $\kappa_2^{(1)}=\kappa_2^{(2)}=0.3$, $f_1^{(2)}=4f_1^{(1)}=0.111$, $b_1=b_2=0.33$ and $b_c=30\,\mu\mathrm{m}$. (—) Stable and (——) unstable HBM solutions. (a) $p_1^{(\mathrm{rms})}$, (b) $p_2^{(\mathrm{rms})}$.

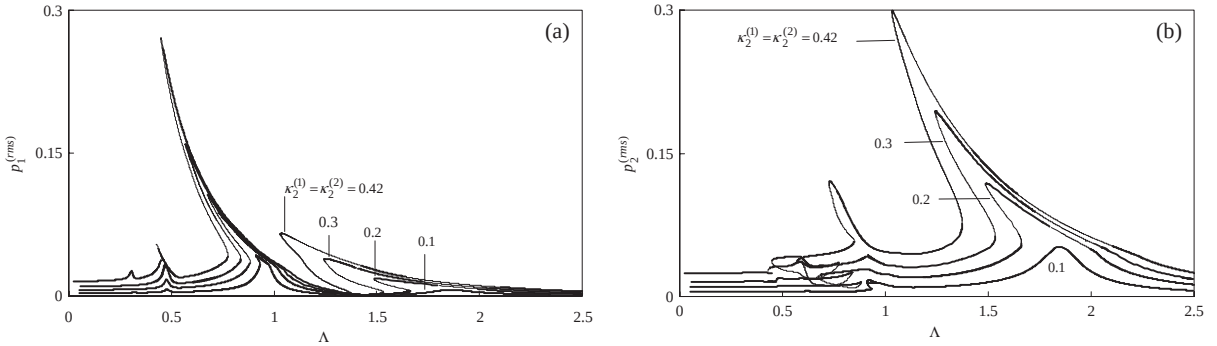

Fig. 8. Influence of the harmonic stiffness parameter for $R=3$, $\zeta=0.05$, $K=1$, $\omega_{n2}\approx 2\omega_{n1}=1.86$, $f_1^{(2)}=4f_1^{(1)}=0.185$, $b_1=b_2=1$ and $b_c=30\,\mu\mathrm{m}$. (—) Stable and (——) unstable HBM solutions. (a) $p_1^{(\mathrm{rms})}$, (b) $p_2^{(\mathrm{rms})}$.

very small. When the damping is very low ($\zeta=0.02$), on the other hand, vibration amplitudes reach levels comparable to the total backlash values to initiate backside collisions (DSI). This causes a hardening type bend at the tips of both primary resonance peaks. This is again in qualitative agreement with a number of single gear pair studies. Also noticed in Fig. 7 is that reducing damping widens the region of instability, confirming the previous LTV model predictions [18].

The influence of the amplitude of harmonic stiffness functions is illustrated in Fig. 8. Four different harmonic stiffness amplitudes were considered, $\kappa_2^{(1)}=\kappa_2^{(2)}=0.42$, 0.3, 0.2 and 0.1. These values represent the fundamental harmonic amplitudes of the gear mesh stiffness function for gear pairs having an involute contact ratio of 1.5, 1.7, 1.8 and 1.9, respectively. Both $p_1^{(\mathrm{rms})}$ and $p_2^{(\mathrm{rms})}$ amplitudes increase significantly when $\kappa_2^{(1)}=\kappa_2^{(2)}$ values are increased. For $\kappa_2^{(1)}=\kappa_2^{(2)}=0.1$, the system is at the threshold of the nonlinear behavior. A very small jump discontinuity is observed near $\Lambda\approx\omega_{n1}=0.96$ while the system acts linearly near $\Lambda\approx\omega_{n2}$. In Fig. 8, $\zeta=0.05$ for both meshes, and at least $\kappa_2^{(1)}=\kappa_2^{(2)}=0.1$ is required to initiate tooth separations. This agrees with Kahraman and Blankenship [5] who stated that tooth separations in a single gear pair are possible when $2\zeta<\kappa_2$. Jump discontinuities become more drastic as values of $\kappa_2^{(1)}=\kappa_2^{(2)}$ are increased. For

instance, for $\kappa_2^{(1)} = \kappa_2^{(2)} = 0.3$, two stable solutions (a SSI and a no-impact motion) coexist within the ranges $0.55 < \Lambda < 0.8$ and $1.25 < \Lambda < 1.5$. While the separation between the jump-up and jump-down frequencies is the widest when $\kappa_2^{(1)} = \kappa_2^{(2)} = 0.42$, it is also observed that the upper branch (SSI) motions become unstable at lower amplitudes. Numerical integration results for this case indicated that the system goes through period-doubling bifurcations as Λ is reduced on the upper branch. Such period-n sub-harmonic motions of the same physical system are investigated in a companion paper [21].

It is also evident from Fig. 8 that the instability region near $\Lambda \approx \omega_{n1}$ due to a parametric resonance widens as the value of $\kappa_2^{(1)} = \kappa_2^{(2)}$ is increased. While there is no unstable period-1 motion at $\Lambda \approx \omega_{n1}$ for a harmonic stiffness amplitude of 0.1, the period-1 motions are unstable within $1.65 < \Lambda < 2.1$ for $\kappa_2^{(1)} = \kappa_2^{(2)} = 0.42$. This is in qualitative agreement with the previous LTV model predictions [18].

In Figs. 5 to 11, the parametric excitations $\kappa_1(t)$ and $\kappa_2(t)$ were assumed to be in mesh and have the same fundamental frequency. The same case of Fig. 2 is considered with different phase angles Γ between $\kappa_1(t)$ and $\kappa_2(t)$, where $\Gamma = 0$, $\pi/2$ and π were considered. In Fig. 9, it is shown that Γ is

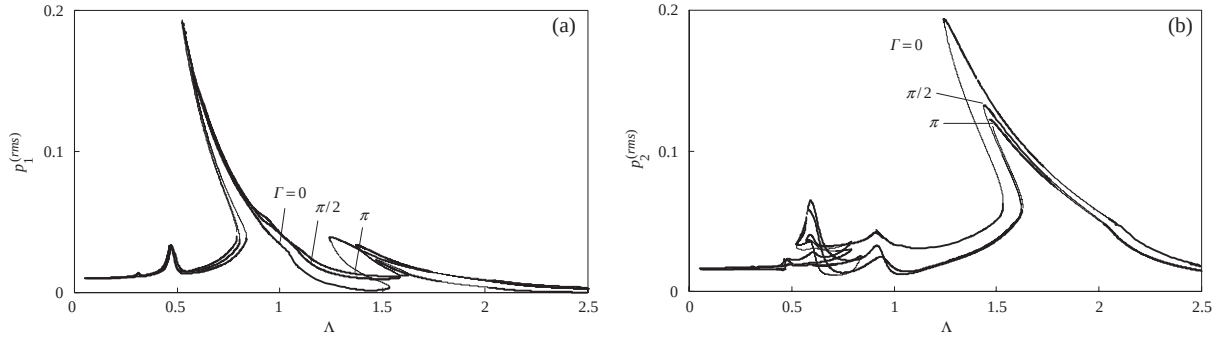

Fig. 9. Influence of the meshing phase angle on $p_j^{(\mathrm{rms})}$ for $R = 3$, $\zeta = 0.05$, $K = 1$, $\kappa_2^{(1)} = \kappa_2^{(2)} = 0.3$, $\omega_{n2} \approx 2\omega_{n1} = 1.86$, $f_1^{(2)} = 4f_1^{(1)} = 0.185$, $b_1 = b_2 = 1$ and $b_c = 30\,\mu\mathrm{m}$. (—) Stable and (——) unstable HBM solutions. (a) $p_1^{(\mathrm{rms})}$, (b) $p_2^{(\mathrm{rms})}$.

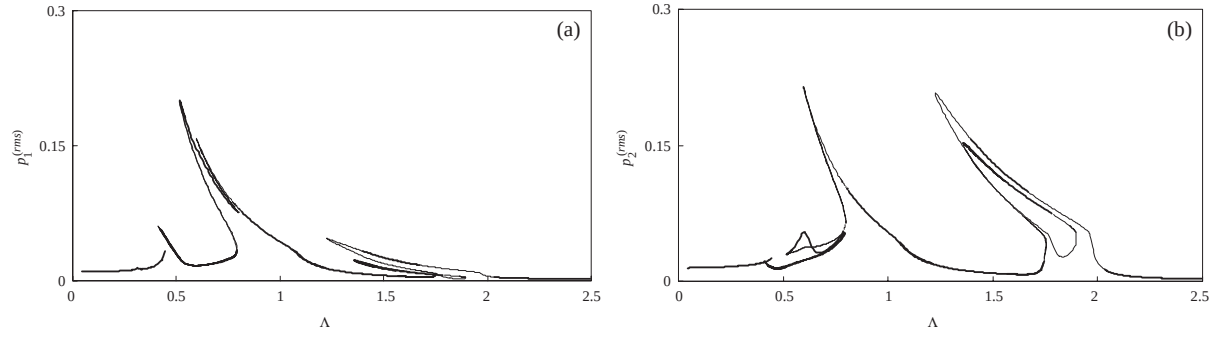

Fig. 10. The rms values of period-1 motions for a tooth mesh frequency ratio of $n = 2$ for $R = 3$, $\zeta = 0.05$, $K = 1$, $\kappa_2^{(1)} = \kappa_2^{(2)} = 0.3$, $\omega_{n2} \approx 2\omega_{n1} = 1.86$, $f_1^{(2)} = 4f_1^{(1)} = 0.185$, $b_1 = b_2 = 1$ and $b_c = 30\,\mu\mathrm{m}$. (—) Stable and (——) unstable HBM solutions. (a) $p_1^{(\mathrm{rms})}$, (b) $p_2^{(\mathrm{rms})}$.

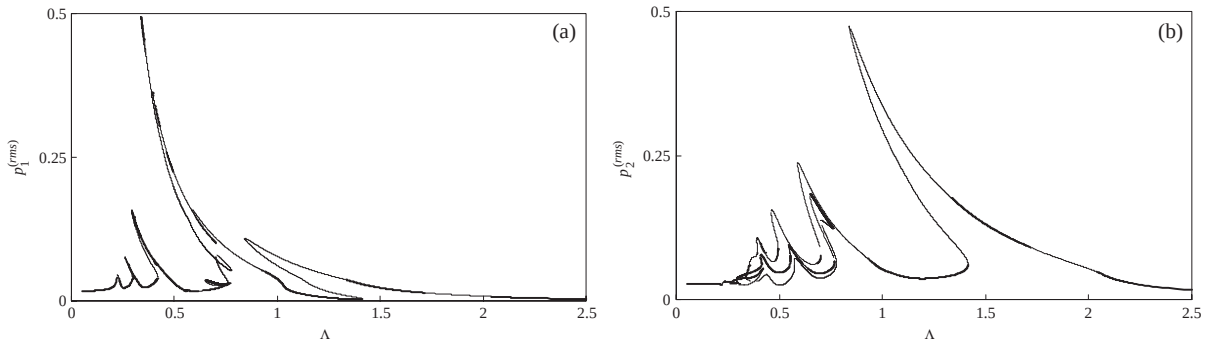

Fig. 11. Period-1 motions for $R = 3$, $\zeta = 0.05$, $K = 3$, $\kappa_2^{(1)} = \kappa_2^{(2)} = 0.3$, $\kappa_4^{(1)} = \kappa_4^{(2)} = -0.18$, $\kappa_6^{(1)} = \kappa_6^{(2)} = 0.04$, $\omega_{n2} \approx 2\omega_{n1} = 1.86$, $f_1^{(2)} = 4f_1^{(1)} = 0.185$, $b_1 = b_2 = 1$ and $b_c = 30\,\mu\text{m}$. (—) Stable and (——) unstable HBM solutions. (a) $p_1^{(\text{rms})}$, (b) $p_2^{(\text{rms})}$.

another parameter influencing vibration amplitudes. The $p_1^{(\text{rms})}$ and $p_2^{(\text{rms})}$ amplitudes are the largest when $\kappa_1(t)$ and $\kappa_2(t)$ are in phase ($\Gamma = 0$). Similarly when the fundamental frequencies of $\kappa_1(t)$ and $\kappa_2(t)$ are different ($n = Z_2/Z_3 \neq 1$), the response is changed considerably. As an example of such a case, Fig. 10 illustrates the response corresponding to the system of Fig. 2 except now $n = 2$. In this case, the gear mesh frequencies are $f_{\text{mesh1}} = \Lambda$ and $f_{\text{mesh2}} = n\Lambda = 2\Lambda$. In Fig. 10, two primary resonance peaks corresponding to $f_{\text{mesh1}} = \omega_{n1}$ and $f_{\text{mesh2}} = \omega_{n2}$ are located at nearly the same frequency since $\omega_{n2} \approx 2\omega_{n1}$ in this particular example. As a result two resonance peaks are combined near $\Lambda = \omega_{n1} = 0.93$ to form the total response. Meanwhile, near $\Lambda = \omega_{n2} = 1.86$, the other primary resonance corresponding to $f_{\text{mesh1}} = \omega_{n2}$ coincides nearly with the parametric resonance corresponding to $f_{\text{mesh1}} = 2\omega_{n1}$, again causing one resonance peak to lay on top of the other.

Finally, Fig. 11 shows the $p_1^{(\text{rms})}$ and $p_2^{(\text{rms})}$ response spectra corresponding to periodic $\kappa_1(t)$ and $\kappa_2(t)$. In this case, $\kappa_2^{(\ell)} = 0.3$, $\kappa_4^{(\ell)} = -0.18$, $\kappa_6^{(\ell)} = 0.04$ in Eq. (9) with $K = 3$. This corresponds to a gear pair having an involute contact ratio of 1.7 [25] meaning that on average 1.7 tooth pairs remain in contact. Since $\omega_{n2} \approx 2\omega_{n1}$ in this case, inclusion of the higher harmonics of the mesh stiffness excitations pose additional complications. The primary resonance due to the fundamental harmonic at $\Lambda = \omega_{n2}$ also corresponds to the parametric resonance due to the fundamental harmonic at $\Lambda = 2\omega_{n1}$ and the parametric resonance due to the first harmonic at $\Lambda = 2(\frac{1}{2}\omega_{n2}) = \omega_{n2}$. Similarly, primary resonance due to the first-harmonic amplitude of mesh stiffnesses at $\Lambda = \frac{1}{2}\omega_{n2}$ coincides with the primary resonance frequency due to the fundamental harmonic at $\Lambda = \omega_{n1}$ In addition, some of these frequencies represent super-harmonic resonances as well. Therefore, the response amplitudes and the severity of the jump discontinuities near $\Lambda = \omega_{n1}$ and $\Lambda = \omega_{n2}$ are increased significantly. Also noted in these figures is that the period-1 motions lose stability quite erratically on the upper branches of the primary jumps. Bifurcation diagrams obtained numerically for these upper branch motions, as shown in Fig. 12, reveal many sub-harmonic and chaotic motions, period-doubling cascades and other nonlinear phenomena. For instance, complete period-doubling and period-halving bifurcations of period-2^m motions (m: integer) surround a chaotic frequency band as shown in Fig. 12(a). Similarly, other

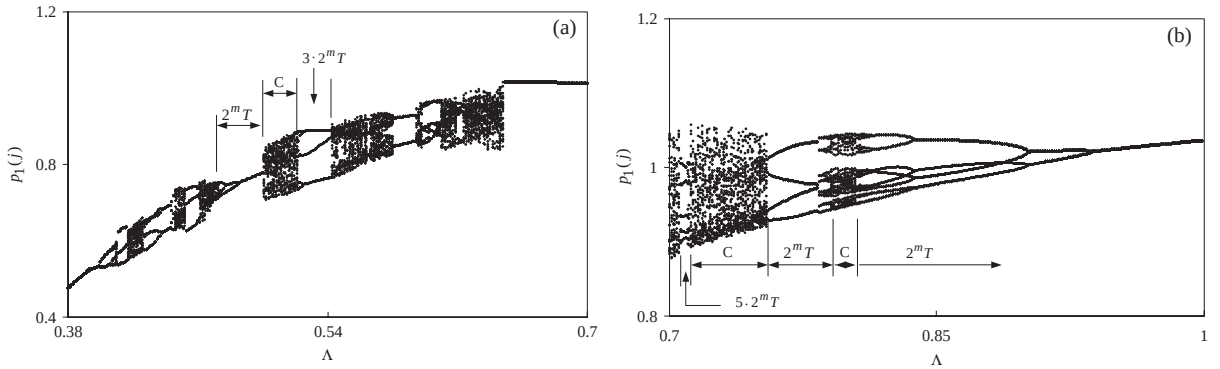

Fig. 12. Bifurcation diagram of $p_1(t)$ on the upper branch of Fig. 11(a) within (a) $0.38<\Lambda<0.7$ and (b) $0.7<\Lambda<1.0$ indicating period-1, period-2^m, $3\cdot 2^m$ $5\cdot 2^m$, and chaotic (C) motions.

period-$3\cdot 2^m$ (3 T, 6 T, 12 T, etc.) and period-$5\cdot 2^m$ (5 T, 10 T, etc.) period-doubling routes to chaos are also evident from Fig. 12(a) and (b). Such motions are investigated in a companion paper [21].

One observation from the results presented up to this point is that the coupling between the two gear meshes is rather weak. A non-linearity applied at one mesh appears to impact only one of the primary resonance peaks significantly, while the other peak influenced more by the non-linearities applied to the second gear mesh. This issue of modal coupling must be investigated further to determine whether this observation is a general one that is valid for all typical multi-mesh gear systems. For this purpose, the model must be modified to include torsional flexibilities of the shafts as well. Our ongoing investigations focuses on this, as well as on time-varying systems having piecewise nonlinear displacement functions.

5. Conclusion

A non-linear time-varying dynamic model of a drive train consisting of three shafts and two gear pairs was proposed in this study. The lumped parameter dynamic model included the gear backlash non-linearities and parametrically varying gear mesh stiffnesses dictated by the gear contact ratios. Dimensionless equations of motion were solved for the steady-state period-1 response by using a multi-term Harmonic Balance Method (HBM) in conjunction with discrete Fourier Transforms. The HBM solutions were shown to be accurate by comparing them to direct numerical integration solutions. Floquet theory was applied to determine the stability of the steady state HBM solutions. An example gear train was modeled to show the sensitivity of the response to alternating mesh stiffness amplitudes, gear mesh damping, static torque transmitted, and the gear mesh frequency ratio. Based on the results of the parametric study presented in the previous section, several general conclusions can be made including the following:

- The multi-mesh gear system studied exhibits a variety of nonlinear behavior. The period-1 motions follow the softening type of jump discontinuities at the primary and parametric resonance frequencies of the corresponding LTV system. This is mainly due to loss of contact of mating teeth resulting in instants of zero gear mesh stiffness.

- Given typical ranges of system parameters, no back collisions (double-sided impacts) were observed.
- It was shown that neglecting gear backlash non-linearity by forcing the teeth to stay in contact, as it is done by previous LTV models, would result in inaccurate predictions near these resonance frequencies while the behavior away from primary, super-harmonic and sub-harmonic (parametric) resonance frequencies is still linear-time-varying.
- No combination resonance and a very limited super-harmonic resonance were observed again within the typical ranges of parameters.
- A weak modal coupling between the two gear meshes was noted. Any backlash introduced in one mesh influences only one of the primary resonance peaks of the system greatly while the non-linearity in the vicinity of the other primary resonance peak may be attributable to the non-linearities introduced in the other mesh. This, at least within the parameter ranges studied, allows considering one non-linearity at a time while predicting the response near the corresponding primary resonance peak.
- This study also demonstrates that the period-n sub-harmonic motions should be expected to play a significant role in the areas of parametric resonance frequencies, especially when the system is lightly damped and the mesh stiffness amplitudes are significant.

Acknowledgements

The authors thank Hashemite University, Jordon and the University of Toledo for supporting the first author during this study.

References

[1] H.N. Özgüven, D.R. Houser, Mathematical models used in gear dynamics—a review, *Journal of Sound and Vibration* 121 (1988) 383–411.
[2] G. W. Blankenship, R. Singh, A comparative study of selected gear mesh interface dynamic models, *Proceedings of the Sixth International Power Transmission and Gearing Conference*, Phoenix, 1992, pp. 137–147.
[3] A. Kahraman, R. Singh, Non-linear dynamics of a spur gear pair, *Journal of Sound and Vibration* 142 (1990) 49–75.
[4] G.W. Blankenship, A. Kahraman, Steady state forced response of a mechanical oscillator with combined parametric excitation and clearance type non-linearity, *Journal of Sound and Vibration* 185 (1994) 734–765.
[5] A. Kahraman, G.W. Blankenship, Interactions between commensurate parametric and forcing excitations in a system with clearance, *Journal of Sound and Vibration* 194 (1996) 317–335.
[6] H. Vinayak, R. Singh, C. Padmanabhan, Linear dynamic analysis of multi-mesh transmissions containing external rigid gears, *Journal of Sound and Vibration* 185 (1995) 1–32.
[7] J.P. Raclot, P. Velex, Simulation of the dynamic behaviour of single and multi-stage geared systems with shape deviations and mounting errors by using a spectral method, *Journal of Sound and Vibration* 220 (1999) 861–903.
[8] T.C. Lim, J. Li, Dynamic analysis of multi-mesh counter-shaft transmission, *Journal of Sound and Vibration* 219 (1999) 905–918.
[9] H. Iida, A. Tamura, K. Kikuchi, H. Agata, Coupled torsional–flexural vibration of a shaft in a geared system of rotors (1st report), *Bulletin of the JSME* 23 (1980) 2111–2117.
[10] H. Iida, A. Tamura, M. Oonishi, Coupled torsional-flexural vibration of a shaft in a geared system (3rd report), *Bulletin of the JSME* 28 (1985) 2694–2698.

[11] H. Iida, A. Tamura, H. Yamamoto, Dynamic characteristics of a gear train system with softly supported shafts, *Bulletin of the JSME* 29 (1986) 1811–1816.
[12] T. Iwatsubo, S. Arii, R. Kawai, Coupled lateral-torsional vibration of rotor system trained by gears, *Bulletin of the JSME* 27 (1984) 271–277.
[13] K. Umezawa, T. Ajima, H. Houjoh, Vibration of three axis gear system, *Bulletin of JSME* 29 (1986) 950–957.
[14] M. Kubur, A. Kahraman, D. Zini, K. Kienzle, Dynamic analysis of multi-mesh helical gear sets by finite elements, *Journal of Vibration and Acoustics* 126 (2004) 398–406.
[15] C. S. Hsu, W. H. Cheng, Steady state response of a dynamical system under combined parametric and forcing excitations, *Journal of Applied Mechanics* (1974) 371-378.
[16] M. Benton, A. Seireg, Factors influencing instability and resonances in geared systems, *Journal of Mechanical Design* 103 (1981) 372–378.
[17] W. Mollers, Parametererregte Schwingungen in einstufigen Zylinderradgetrieben, PhD Dissertation, Rheinisch-Westfalischen Technischen Hochschule Aachen, 1982.
[18] J. Lin, R.G. Parker, Mesh stiffness vibration instabilities in two-stage gear systems, *Journal of Vibration and Acoustics* 124 (2002) 68–76.
[19] A. Kahraman, G.W. Blankenship, Experiments on nonlinear dynamic behavior of an oscillator with clearance and periodically time-varying parameters, *Journal of Applied Mechanics* 64 (1997) 217–226.
[20] O.O. Sato, H. Shimojima, S. Inano, Dynamic torsional analysis of gear train system, *Bulletin of JSME* 28 (1985) 1756–1780.
[21] A. Al-shyyab, A. Kahraman, Non-linear dynamic analysis of a multi-mesh gear train using multi-term harmonic balance method: subharmonic motions, *Journal of Sound and Vibration* 279 (2005) 417–451.
[22] Y.S. Choi, S.T. Noah, Forced periodic vibration of parametric piecewise-linear system, *Journal of Sound and Vibration* 121 (1988) 117–126.
[23] A.V. Oppenhiem, R.W. Schaffe, *Digital Signal Processing*, Prentice-Hall, Englewood Cliffs, NJ, 1975.
[24] S. Rudiger, *Practical Bifurcation and Stability Analysis*, 2nd Edition, Sprigner, New York, 1994.
[25] A. Kahraman, G.W. Blankenship, Effect of involute contact ratio on spur gear dynamics, *Journal of Mechanical Design* 121 (1999) 112–118.